Chapter-4 Structural and Electrical Properties of Y-doped..

4.1 Introduction

Perovskite-type oxides (ABO_3) are promising candidates as anode for SOFCs and sensor as well due to their mixed ionic/electronic (electrical) conductivity with good catalytic activity [14], [142], [143]. Pure $SrTiO_3$ perovskite cannot be used as anode due to its low electrical conductivity, whereas donor doped $SrTiO_3$ systems are proposed to be suitable to anodic conditions due to their chemical and thermal stability, high electrical conductivity and carbon/sulphur tolerance [36]. In literature, several attempts have been made to use Y-doped $SrTiO_3$ with A-site deficient stoichiometry as anode in a solid oxide fuel cell for e.g. $Y_{0.07}Sr_{0.895}TiO_3$ has been utilized as anode in an electrolyte-supported fuel cell [144]. Further, $Y_{0.08}Sr_{0.88}TiO_3$ was used to impregnate a backbone of YSZ electrolyte supported SOFC [145] and YST-SDC composite impregnated by Ni to act as a catalyst [146].

It is well known that in $SrTiO_3$ based systems, the oxidation of fuel occurs at triple phase boundary region and mixed conductivity feature provides oxidizing reaction sites that decrease the polarization and accelerate the anode reaction [37]. However, the combination of ionic and electronic conductivity could not satisfy the requirements for the electrode materials, therefore, many efforts have been made to enhance the conductivity of the various materials. It is reported that the acceptor doping in the perovskite materials enhances the ionic conductivity [38], [147] whereas, the donor doping increases the electronic conductivity [37]. Yttrium acts as donor dopant for the $SrTiO_3$, and suitable for substitution due to less difference between ionic radii of Y^{3+} (1.22 Å, CN 12) and Sr^{2+} (1.44 Å, CN 12). As the results of doping, two phenomena occur simultaneously, first maintain electro-neutrality in lattice defect structure due to

charge imbalance between Y^{3+} & Sr^{2+} and second improve the electrical conductivity of $SrTiO_3$ *via* the formation of oxygen-rich planes. In addition to that, redox coupling between Ti^{4+} and Ti^{3+} that also occurs in the system contributes to improving the electrical conductivity under reducing atmosphere and shows an n-type semiconducting behaviour [40]–[42], [148].

In present chapter, a systematic investigation on Y^{3+} doped $SrTiO_3$ ($Y_xSr_{1-x}TiO_{3-\delta}$ with x = 0, 0.03, 0.05, 0.08 and 0.10) was performed and results obtained were analysed. Samples were synthesized *via* citrate-nitrate auto-combustion route using citric acid as fuel agent. The effect of Yttrium (Y^{3+}) doping on electrical conductivity in $SrTiO_3$ under air and H_2 atmospheres was investigated through electrochemical impedance measurements.

4.2 Results and Discussion

4.2.1 Structural Studies

The XRD patterns of the sintered samples of the system $Y_xSr_{1-x}TiO_3$ (with x = 0.0, 0.03, 0.05, 0.08 and 0.10) assigned as YST0, YST3, YST5, YST8 and YST10 respectively, are shown in fig. 4.1 (a). To check the symmetry, Rietveld refinement was carried out using FULL PROF Suite software package with Pseudo-Voigt wave function. From the best fit, χ^2 values are mentioned in table 4.1. It is observed that all the samples show cubic phase with space group $Pm\bar{3}m$ (JCPDS Card Number: 86-0178). In the samples with $x \leq 0.03$ no impurity peaks are detected, while for $x \geq 0.05$, secondary phase $Y_2Ti_2O_7$ (JCPDS Card Number: 87-1849) is observed. It is also observed that the diffraction peaks shift towards higher angle as the concentration of Yttrium is increased as shown in fig. 4.1 (b) which clearly indicates that the lattice parameters are decreasing continuously. There may be two factors responsible for decrease in lattice parameters.

First, incorporation of Y^{3+} on Sr sites that leads to decrease lattice parameters due to smaller ionic radii of Y^{3+} (1.22 Å, CN 12) as compared to Sr^{2+} (1.44 Å, CN 12). Secondly, increasing amount of secondary phase $Y_2Ti_2O_7$ which may increase the defects such as oxygen vacancies, lattice disorders etc. in the samples with x > 0.03 and which are removed on sintering leading to lattice contraction [149]. Similar kind of decreasing behaviour in lattice parameter has been reported by other authors [150].

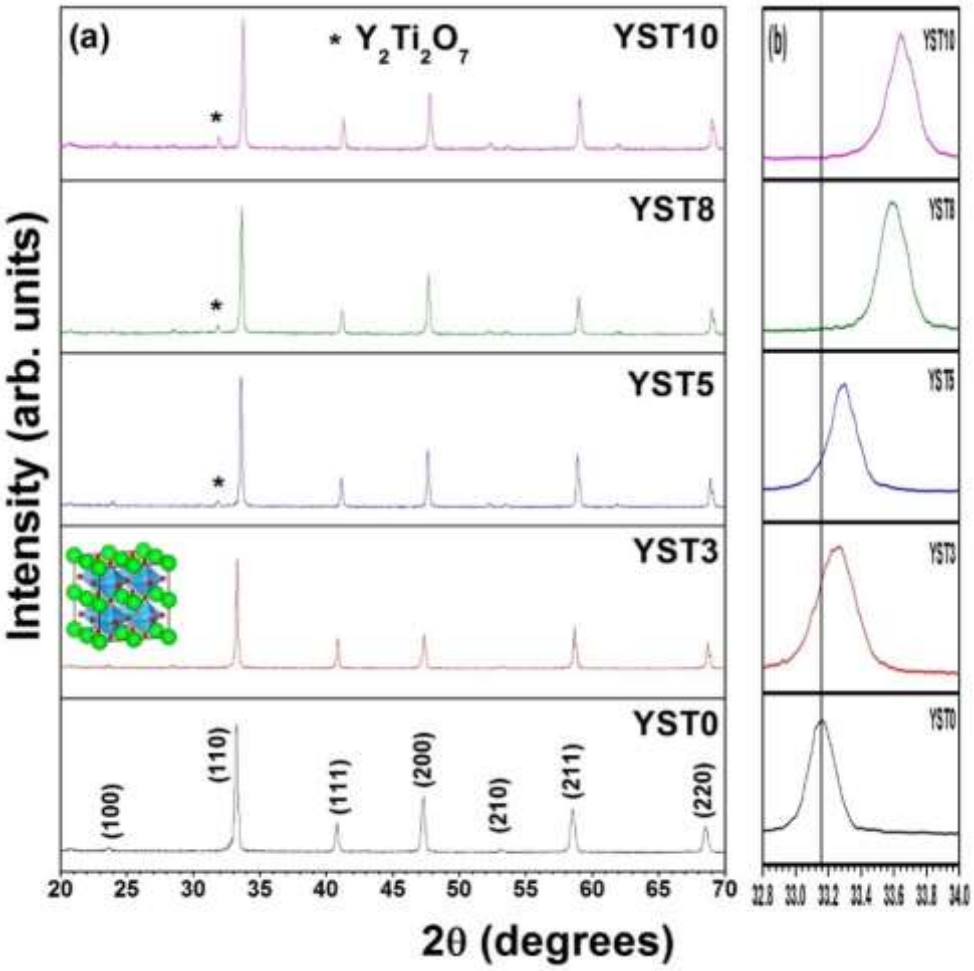

Figure 4.1: (a) XRD patterns of the sintered samples of the system $Y_xSr_{1-x}TiO_3$ (i.e, YST0, YST3, YST5, YST8, and YST10) (b) Angle shift of (110) peak with the Y doping.

However, more complex incorporation mechanisms might take place (see below), with the same effect on lattice constant. The Reference Intensity Ratio (RIR) method was used to calculate the concentration of secondary phase [148]. RIR relates the

concentration of phases (X_i) in a sample with the intensity of the highest peak (I_i) of each phase, obtained by XRD through tabulated RIR_i coefficient defined as:

$$RIR_i = R_i = I_i/I_c \quad (4.1)$$

where I_c is the corundum intensity in 50:50 mixture with phase i. Therefore, the concentration of secondary phase, X_s, can be calculated by equation:

$$X_p/X_s = I_p/I_s \cdot R_s/R_p \quad (4.2)$$

where p and s are referred, respectively to main and secondary phase and X_p is the concentration of the main phase. In this case, R_p and R_s are equal to 7.32 and 7.89, respectively. X_s values, as function of $x \geq 0.03$ in $Y_xSr_{1-x}TiO_{3-\delta}$ are reported in fig. 4.2 (a). It is observed that X_s increases by increasing amount of yttrium doping.

The lattice parameters of the studied systems are also plotted with the function of tolerance factors using eq. (1.5) as shown in fig. 4.2 (b). From table 4.1, it is observed that the unit cell volume decreases with increase in Y content, which may be attributed to the replacement of the Sr cation by incorporation of Y^{3+} within the perovskite structure [148].

Figure 4.2 (c) shows the variation of intensity of XRD peak with 2θ-δ (^{o}) where δ is the angle at which maxima occurs showing diffuseness of XRD peak (110) with the compositions and observed that the diffuseness of XRD peak increases towards left with the Y^{3+} substitution in $SrTiO_3$. The increase in diffuseness is due to the formation of polarons in the matrix [140]. Microstrain and crystallite size of the samples were calculated from XRD results by using Williamson-Hall model [82] as given by eq. (2.1).

Figure 4.2 (d) shows the variation of microstrain and crystallite size with the compositions. It is observed that value of microstrain and crystallite size showed the similar trend i.e. they are maximum for YST5, whereas, the microstrain and crystallite size decrease for YST3 and YST8.

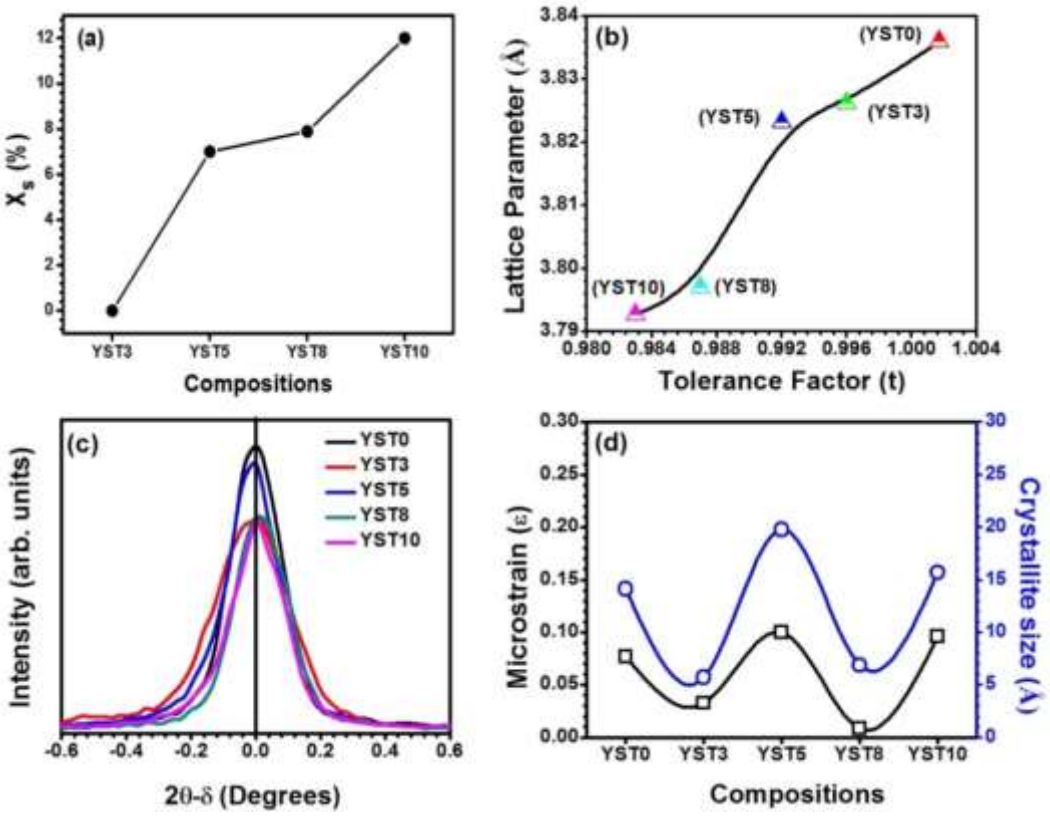

Figure 4.2: (a) Secondary phase concentration, X_s, as function of $x \geq 0.03$ in $Y_xSr_{1-x}TiO_{3-\delta}$ (b) Variation of lattice parameter with tolerance factor, (c) The variation of intensity of XRD peak (110) via 2θ-δ (^{o}) with compositions (x) for $Y_xSr_{1-x}TiO_{3-\delta}$ system, and (d) The variation of microstrain and crystallite size with compositions (x).

FESEM images in fig. 4.3, reveal that grains and grain boundary are clearly formed in YST5, whereas, its formation in other compositions are relatively weak. Maximum microstrain and crystallite size in YST5 could be due to the enhanced grain-to-grain interactions as shown in FESEM images. It may be caused by the generation of high amount of stress concentration and local distortions under high sintering temperature [151].

4.2.2 Microstructural Analysis

FESEM images of fractured samples, sintered at 1200 ^{o}C in air, are shown in fig. 4.3 (a)-(e). YST8 sample appears the most porous among all compositions, and that finding was confirmed with the value of density measured by Archimedes method as

reported in table 4.1. The average grain sizes of compositions YST0, YST3, YST5, YST8 and YST10 were found to be 2.19 µm, 1.15 µm, 3.67 µm, 1.55 µm, and 3.87 µm, respectively. Along with the formation of dense grains, water-mark and lamellar features are also observed in dense micrographs as illustrated in fig. 4.3 (c and e). This non-monotonous behavior of grain size and density is coherent with the crystallite size and microstrain behavior, reported in the fig. 4.2 (d).

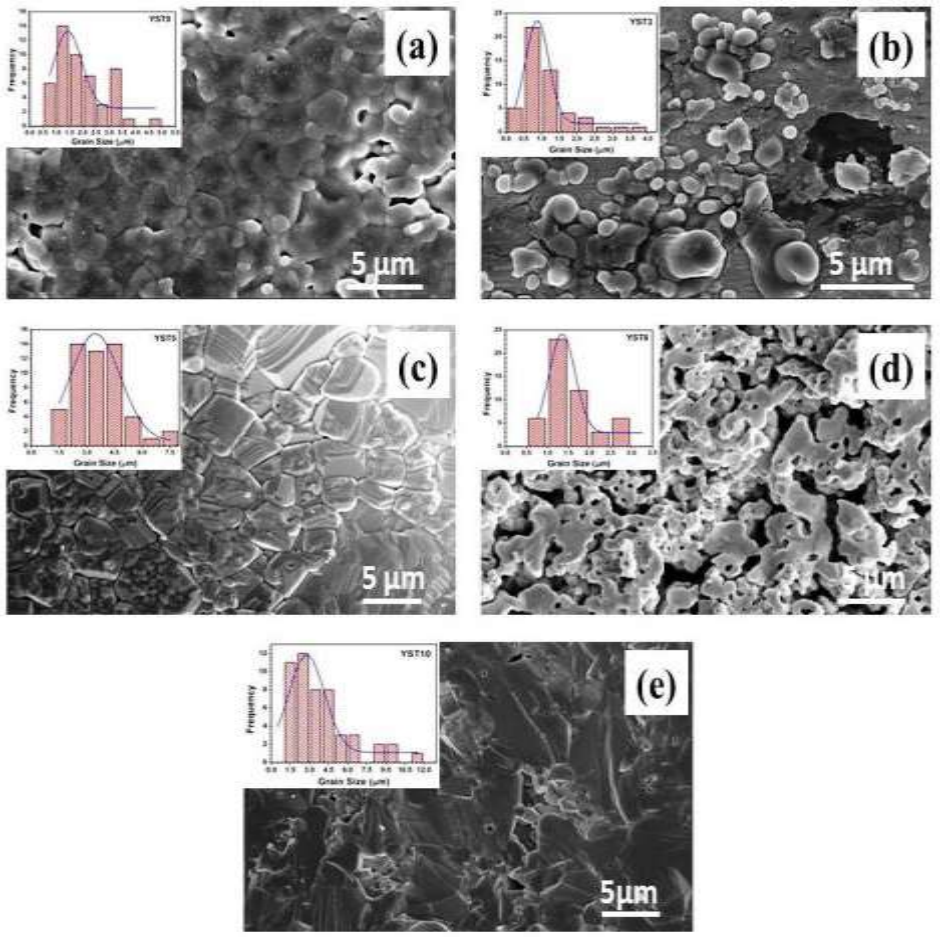

Figure 4.3: FESEM images of fractured samples sintered at 1200 ^{o}C in air for (a) YST0 (b) YST3 (c) YST5 (d) YST8 and (e) YST10.

4.2.3 XPS Analysis

The oxidation states of constituent elements are analysed using X-ray Photoelectron Spectroscopy (XPS) technique. Figure 4.4 (a) shows the XPS wide spectra of Y doped $SrTiO_3$ samples. The entire XPS spectrum consists of core and satellite binding energy

peaks of constituent elements including C. The binding energy (BE) peaks of the constituents are marked for different doping concentrations Y ($0.0 \leq x \leq 0.10$). The C 1s peak at ~286 eV originates from external contamination or surface-absorbed CO_2. The binding energies were further calculated after calibration with respect to the C1s reference peak. The spectra revealed binding energy peaks of Sr 3d at ~134 eV, Y 3d at ~157 eV, Sr 3p at ~ 269.4 eV, Ti 2p at ~ 459.4 eV, and O 1s at ~ 530.6 eV. Accordingly, the Sr^{2+} state is confirmed by the above mentioned peak positions. With the increase in Y^{3+} doping content, BE values shifted to higher energy. In fig. 4.4 (a), a satellite peak of O (KLL) is also observed at ~741.3 eV [152]. Also, O 1s spectral regions are used to obtain the information regarding the presence of oxygen vacancies in the samples.

The O-1s peaks, observed for all the compositions in the spectrum, are broader and asymmetric in nature. As the peaks are broad in nature, therefore, they may be split into two peaks. These peaks can be attributed to two different types of oxygen species: lattice oxygen and adsorbed oxygen [153]. Figure 4.4 (b) reveals that the sample YST5 has a higher percentage of adsorbed oxygen in comparison to the lattice oxygen as illustrated in table 4.1. Whereas, in all other investigated samples, the percentage of lattice oxygen is more than the adsorbed oxygen.

The oxidation states of all constituent atoms of the samples have been investigated by XPS spectra. The XPS spectra for Ti 2p of YST5 sample is shown in fig. 4.4 (c). The binding energies of Ti $2p_{3/2}$ and Ti $2p_{1/2}$ for the YST5 sample are 458.3 and 464.2 eV respectively as shown in fig. 4.4 (c). These ions exhibit n-type semiconducting behaviour due to redox coupling of Ti^{4+}/Ti^{3+} and increase the electrical conductivity as reported by Fuentes et. al [154].

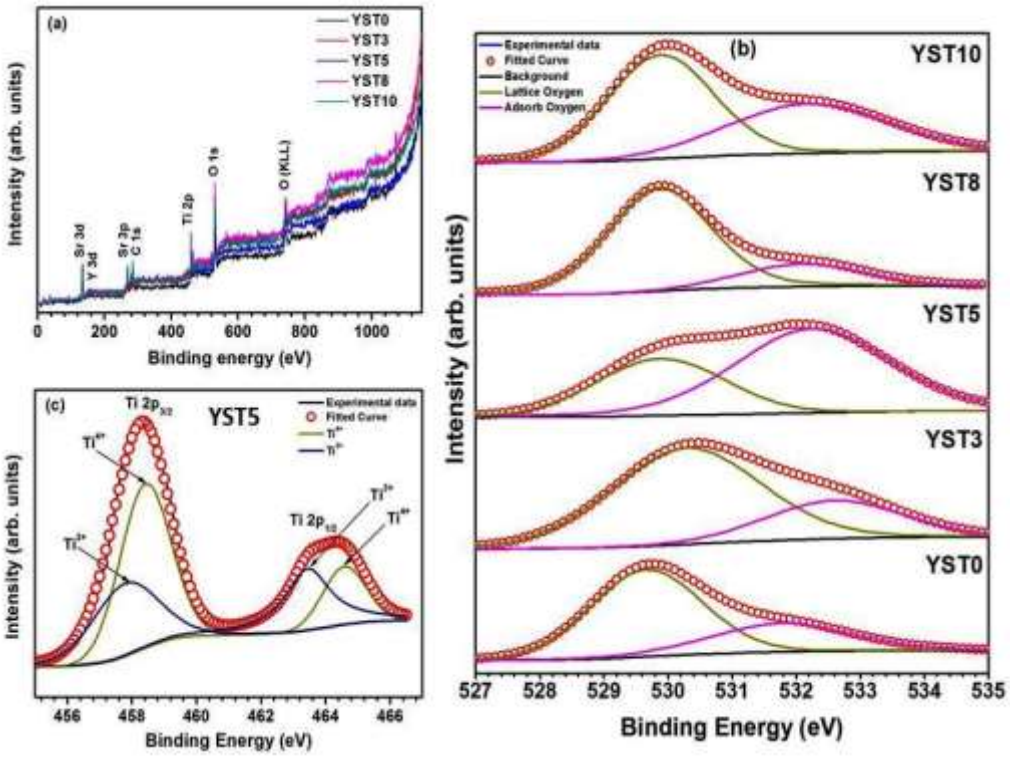

Figure 4.4: (a) The XPS survey spectra of Y doped $SrTiO_3$ (b) The O-1s core level spectra (c) The XPS spectra of Ti 2p of YST5 sample.

4.2.4 Impedance Analysis

From spectra obtained by impedance spectroscopy, in both air and hydrogen atmosphere, the total resistance (R_t) was obtained as the intercept of depressed semi-circular arc on the real axis at low frequency. The total conductivity of the samples was calculated by applying the formula:

$$\sigma = 1/R_t \cdot l/S \tag{4.3}$$

where σ is the conductivity, l is the thickness of pellet and S is the surface area of the pellet. To analyse the mechanism of conductivity, activation energy (E_a) was calculated for each regime in air as well as in reducing atmosphere by using the relation

$$\sigma = \sigma_0/T \cdot \exp(-E_a/kT) \tag{4.4}$$

where σ_o is a pre-exponential factor, E_a is the activation energy for conduction, k is the Boltzmann constant and T is the absolute temperature.

In fig. 4.5 (a) and (b), the Arrhenius plots of log σT *vs.* 1000/T are reported for all compositions in air and hydrogen atmosphere, respectively.

It is observed that the conductivity of each composition increases in hydrogen in comparison to that of the air. YST5 showed the highest conductivity in air whereas YST8 in H_2 atmosphere. The total conductivity of all reduced samples mostly reflects the electronic conductivity because the oxygen vacancies have the lower mobility as compared to electrons in the Y-doped $SrTiO_3$ system. However, the Arrhenius plots, i.e. graph between log (σ.T) and 1000/T exhibit the two slopes in the two temperature ranges (fig. 4.5). At the lower temperature range i.e. 200 to 400 ºC, the linear trend is observed implying the n-type semiconductor like conduction behaviour, while change of slope at higher temperature range i.e. 400 to 700 ºC indicates the polaron hopping conduction mechanism along with oxygen ion conductivity [40], [140].

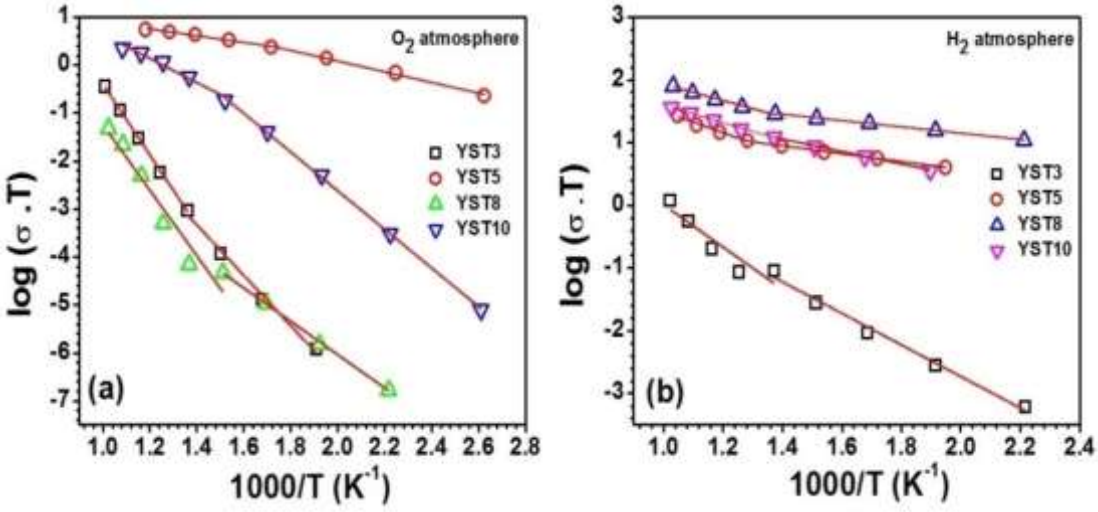

Figure 4.5: The Arrhenius plot of log σT vs. 1000/T (a) in O_2 atmosphere (b) in H_2 atmosphere.

The activation energy calculated for all compositions is listed in table 4.1. It can be noted that in air, E_a values are low for samples YST5 and YST10, suggesting electronic nature of conductivity, especially in the high temperature range.

Table 4.1: Activation energy, relative density and adsorbed oxygen of YST samples.

Sample	χ^2	Volume ($Å^3$)	Relative Density (%)	Adsorbed Oxygen (%)	E_a (eV) O_2 atmosphere		E_a (eV) H_2 atmosphere	
					200-400 °C	400-700 °C	200-400 °C	400-700 °C
YST3	7.69	56.015	68	26.4	1.043	1.465	0.511	0.668
YST5	7.78	55.883	92	65.9	0.222	0.139	0.124	0.332
YST8	7.78	54.742	66	19.5	0.689	1.355	0.100	0.259
YST10	7.81	54.556	95	41.3	0.800	0.497	0.197	0.279

The activation energy is further lowered after reduction in H_2 atmosphere. For all the samples, the activation energy has been found to be in the range of 0.1 to 0.2 eV except for the YST3 sample where E_a exceeds 0.5 eV.

Above reported experimental observations can be explained by considering the incorporation mechanisms of dopant into the perovskite structure of $SrTiO_3$. The average value of ionic radius for Y^{3+} in 6-fold coordination (0.90 Å) and in 12-fold coordination (1.22 Å) [153], three types of incorporation can be considered and expressed by the following equations written in the Kröger-Vink notation:

$$Y_2O_3 + 2TiO_2 \xrightarrow{SrTiO_3} 2Y_{Sr}^{\bullet} + 2Ti_{Ti}' + 6O_O^X + \frac{1}{2}O_2 \quad (4.5)$$

$$Y_2O_3 \xrightarrow{SrTiO_3} Y_{Sr}^{\bullet} + Y_{Ti}' + 3O_O^X \quad (4.6)$$

$$Y_2O_3 \xrightarrow{SrTiO_3} 2Y_{Ti}' + V_O^{\bullet\bullet} + 3O_O^X \quad (4.7)$$

Equation (4.5) accounts for the incorporation of Y^{3+} at the Sr-site, with formation of positively charged defects, compensated by electrons or, equivalently, by partial reduction of Ti^{4+} to Ti^{3+}. In the second case, eq. (4.6), the incorporation takes place both at Sr- and Ti-sites, with self-compensation of charges. Finally, eq. (4.7) is relevant to the case of incorporation at the Ti-site with formation of negatively charged defects, compensated by oxygen vacancies.

As already reported in case of $BaTiO_3$ [78], the most energetically favourable incorporation mechanism for Y^{3+} and similar rare-earths like Dy, Er and Gd, is the self-compensation.

However, other factors can also determine the actual incorporation mechanism, the most important being the amount of dopant, the cationic ratio and the temperature. Lattice parameters and strain are determined by the incorporation mechanism so that, minimal local distortion (microstrain) can be expected when Y^{3+} is replacing both (larger) Sr^{2+} and (smaller) Ti^{4+} atoms. The formation of the pyrochlore phase also introduces point defects, namely Ti vacancies, which affect the lattice size and strain state. Therefore, results indicate that for YST3 self-compensation (eq. 4.5) is mainly active, causing limited microstrain and negligible amount of electrons leading to conduction of ionic nature due to oxygen vacancies produced either intrinsically (Schottky disorder) or through the mechanism of eq. (4.7).

Similar considerations hold for YST8 sample, where the small microstrain indicates simultaneous substitution at both cationic sites, which also reflect lower conductivity and high E_a in air. In this sample, the presence of a secondary phase i.e. Ti vacancies in the main phase may account for observed lowering of the unit cell volume.

Mechanism of eq. (4.5) is mainly active in samples YST5 and YST10 as demonstrated by higher conductivity, lower E_a and higher microstrain. XPS analyses are in agreement as a large amount of Ti^{3+} was detected on the surface of YST5 sample.

Under reducing atmosphere, lattice oxygen may be lost and thus oxygen vacancies will be generated as per eq. (1.19). In order to conserve the electro-neutrality, the following equation must be satisfied.

$$[Ti'_{Ti}] = [Y^{\bullet}_{Sr}] + 2[V^{\bullet\bullet}_{O}] \qquad (4.8)$$

Therefore, both extrinsic defects introduced by Y incorporation at Sr-site and intrinsic oxygen vacancies, which are formed under reducing conditions, contribute to the formation of electrons and increase of conductivity. In case of YST8 sample, adsorbed oxygen (i.e. 19.5%) exhibit a minimum value as shown in table 4.1, indicates the presence of high lattice oxygen in the sample. To maintain the electro-neutrality, high amount of defects may generate and they could be compensated by Sr and oxygen vacancies under reducing conditions leading to improvement in electrical conductivity [41]. The conductivity of all samples is actually increased after exposure to hydrogen atmosphere; the higher value reported for sample YST8 can also be attributed to the large porosity (fig. 4.3 (d)) which allowed for a more efficient exchange between the gas phase and solid phase. This also suggests that the reducing stage performed (24 h at 700 °C) was not sufficient to get equilibrium in dense samples. In addition, the porosity can be further increased by incorporation of A-site deficiency like $(Y_{0.08}Sr_{0.92})_{1-x}TiO_{3-\delta}$ and B-site deficiency like $Y_{0.08}Sr_{0.92}Ti_{1-x}O_{3-\delta}$ as reported by several authors [40], [41].

4.2.5 Chemical Stability

To check the chemical stability of the YST samples, XRD measurements were repeated after the reduction. Results are reported in fig. 4.6, together with the patterns obtained after sintering in air as discussed in structural studies. It is observed that the XRD patterns of YST5 to YST10 (fig. 4.6 (b to d)) overlap with each other showing no signs of chemical and structural degradations. Whereas, the sample YST3 (fig. 4.6 (a)) showed the formation of additional secondary phases after reduction. In addition, corresponding FESEM micrographs of reduced samples (inset in fig. 4.6) also confirmed that the sample YST3 strongly degraded with the formation of Ti-Sr mixed oxides. Also, for all the compositions, the peaks have been shifted towards the left in the reducing

atmosphere showing lattice expansion. The lattice expansion might be attributed to increasing the oxygen vacancies concentration under reducing atmosphere.

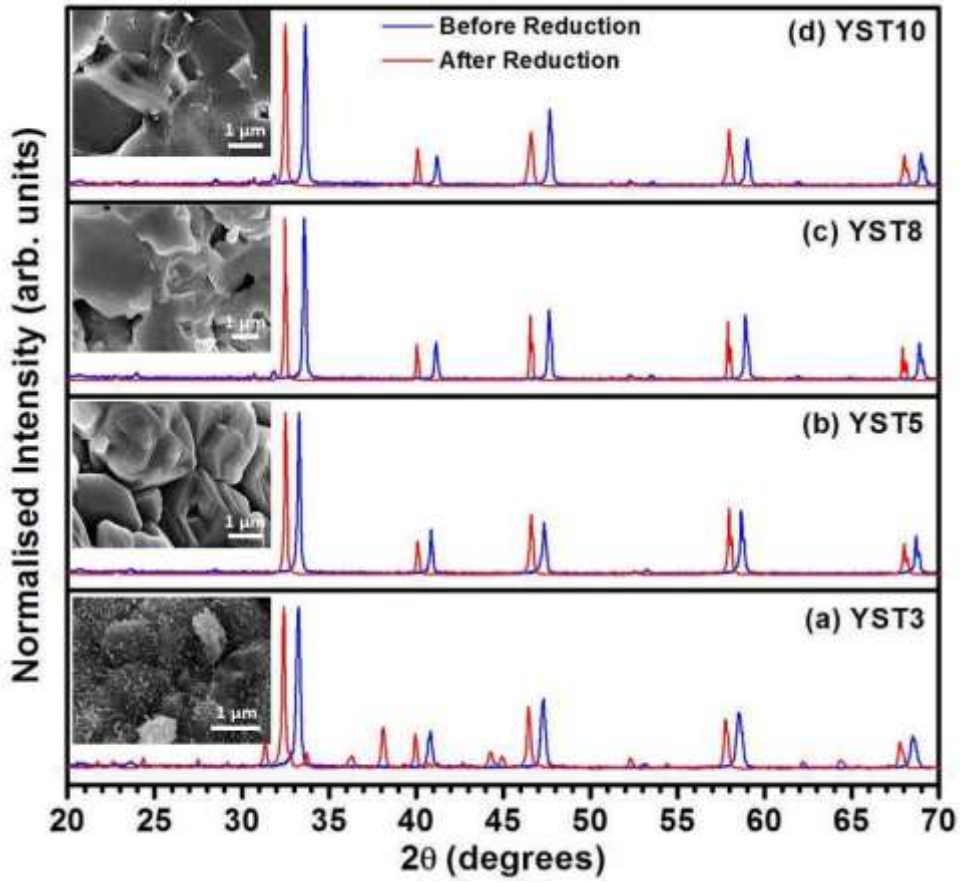

Figure 4.6: XRD patterns of Y-doped $SrTiO_3$ samples before and after reducing atmosphere and inset FESEM micrographs of reduced samples.

Among all the investigated samples, the most promising candidate for use as anodic material in SOFC is $Y_{0.08}Sr_{0.92}TiO_3$ due to its good chemical stability coupled with high conductivity and low activation energy under reducing condition.

4.3 Conclusions

In this chapter, $Y_xSr_{1-x}TiO_3$ system was studied with the change in concentration of yttrium doping. Different incorporation mechanisms are activated, particularly simultaneous incorporation of Y^{3+} at Sr- and Ti-sites or incorporation of Y^{3+} at Sr-site with electron compensation. XPS revealed the confirmation of electron compensation mechanism. Upon reduction, the conductivity increased and the activation energy

decreased to nearly half in all the samples. Also, the sample YST8 was found to be chemically stable with 34% porosity having the highest electrical conductivity under reducing conduction. Whereas, the sample YST3 is strongly degraded. Furthermore, HRTEM measurement may be incorporated to identify the beginning of degradation of the samples as a future work. Hence, YST8 may be considered as a promising anode material for solid oxide fuel cells.